Progress In Electromagnetics Research C, Vol. 119, 97–114, 2022

Multi-Objective Optimization and Analysis of Six-Pole Outer Rotor Hybrid Magnetic Bearing

Gai Liu, Zhihao Ma, Huangqiu Zhu*, Jingbo Sun, and Junqi Huan

Abstract—The multi-objective optimization of the six-pole outer rotor hybrid magnetic bearing (OSHMB) not only solves the nonlinear and strong coupling problems of the three-pole magnetic bearing (THMB), but also makes the magnetic bearing structure more compact and improves the maximum bearing capacity. Firstly, the structure and working principle of the OSHMB are introduced, and the mathematical models of suspension forces are established by the Maxwell tensor method. Secondly, the key parameters of the OSHMB are multi-objective optimized, and an optimal set of parameters is obtained through the sensitivity analysis, constructing the response surface model, and the multi-objective optimization based on the genetic algorithm. Based on the optimal parameters, the force current characteristics and maximum carrying capacity of the OSHMB are analyzed. Finally, the experimental platform is built. The suspension experiments, anti-interference experiments, and load loading experiments are performed. It can be seen that the maximum bearing capacity of the OSHMB is about 9.6% higher than that of the SHMB.

1. INTRODUCTION

The friction between rotor and stator of traditional mechanical bearing increases the energy loss, which can be solved by magnetic bearing [1]. The traditional magnetic bearings have four magnetic poles, and two magnetic poles are driven by one power amplifier, so magnetic bearing requires two power amplifiers [2]. A rotary shaft is supported by two radial magnetic bearings, and the rotary shaft connects with the rotor of a motor [3, 4]. Power amplifier and displacement sensors increase the cost and volume of the magnetic bearing system. Therefore, the compact and cost effective design has long been an important issue in research and development of magnetic bearings. One approach is to use the sensorless control [5–7]. Only one three-phase inverter is required for three-pole magnetic bearings in [8], which greatly reduces the cost and power consumption of the magnetic bearing system. To increase the stability of magnetic bearings, an accurate mathematical model is established in [9]. Although the three-pole magnetic bearing has many advantages, it also increases the overall design and cost of the system in [10].

By optimizing the height ratio of PM, the suspension force of radial high-temperature superconducting magnetic bearing is enhanced [11]. The structure of radial magnetic bearing is optimized by using finite element analysis (FEA) method, and the results are accurate and efficient [12]. The magnetic bearing is constructed using basic unit cubic bulks in [13]. 16 cubic bulks are used as a bearing model to sandwich between top and bottom parts, and the maximum load value is increased. The structure and main parameters are optimized in [14], and the maximum control current can be reduced to only 40% of initial design by the optimization. In [15], a compound control method using an improved non-singular fast terminal sliding mode controller is developed, which can significantly improve the response time and anti-disturbance performance. In [16], the axial size of the magnetic

Received 6 January 2022, Accepted 7 March 2022, Scheduled 22 March 2022
* Corresponding author: Huangqiu Zhu (zhuhuangqiu@ujs.edu.cn).
The authors are with the School of Electrical and Information Engineering, Jiangsu University, Zhenjiang 212013, China.

bearing becomes large, and the dynamic performance of the system is reduced with displacement sensors. The control equations are coupled to each other, causing a complex controller design. The high price of sensors increases the overall cost of magnetic bearings; therefore, a rotor displacement self-detection method is proposed. In [17], after multiobjective optimization, the magnetic bearing can be cheaper and smaller, and the internal space can be reasonably used. In [18], a different approach for using reduced model instead of large order model for controlling axial active magnetic bearing is proposed. In [19], for the optimal use of magnetic materials in passive magnetic bearings, two modifications in a passive magnetic bearing structure are investigated. In [20], the position control problem for the active magnetic bearing suspension system under external disturbance is discussed. In [21], the topology of a switching power amplifier is analyzed and optimized. In [22], considering the incompatible objectives of the optimization model, the method of multiobjective optimization on the bearing is proposed, which can balance these objectives compared with single-objective optimization. In [23], the design principles for different parameters are given, and different magnetic bearing structures are designed. In [24], a superconducting linear magnetic bearing 3D finite element model for a maglev vehicle is developed, and the optimization method is that the 3D model is reduced to a 2D model by shortening its length artificially, instead of decreasing the critical current density. The proposed superconducting magnetic bearing in [25] investigates the vertical force on the rotor as a function of the vertical displacement according to the cooling procedure of the superconductors by using an amperian current approximation based on frequency injection method (FIM). In [26], a design method of the high speed (HS) electrical machine supported by active magnetic bearing (AMB) is described. In [27], the particle swarm optimization and chaotic local search algorithm are combined to optimize the volume, suspension force, eddy current loss, and weight of two degrees of freedom hybrid magnetic bearings. The application of the intelligent optimization algorithms realizes the multi-objective optimization design of magnetic bearings and greatly reduces the time spent in the optimization design. However, these methods of algorithm nesting do not provide the Pareto solution set of multi-objective optimization, and the interaction of each optimization objective cannot be directly observed.

In this paper, a six-pole hybrid magnetic bearing (SHMB) is designed, and its parameters are multi-objective optimized. Its working principle and mathematical model are constructed. A parameter design method is put forward, where the key parameters are obtained. Magnetic flux density is analyzed, and current stiffness and displacement stiffness of OSHMB are tested by finite element analysis, which verify the validity of optimized results. Experimental platform is built. Compared with the SHMB, the OSHMB can increase the suspension force in the same volume, and a more reasonable stator structure is obtained.

2. STRUCTURE AND WORKING PRINCIPLE

A two-piece radial-axial outer rotor SHMB structure studied in this paper is shown in Figure 1(a). There are two radial stators, which are divided into left and right stators. Each stator distributes 6 magnetic poles along the radial direction, 12 in total, and the magnetic poles on the two stator plates are aligned along the axial direction. All 12 radial magnetic poles are wound with control coils to produce suspension force that makes the rotor stable and suspended.

There are two kinds of fluxes, bias flux and control flux in the OSHMB. As depicted in Figure 1(b), the bias flux is generated by the permanent magnet magnetizing along the z direction, and the specific flow direction is from the N pole of the permanent magnet, passing through the left radial stator, left air gap, rotor, right air gap, and right radial stator back to the other pole of the permanent magnet. The control flux is generated by the control coil of each pole and flows only in the side of the corresponding stator.

As can be seen from Figure 1(b), there are two stators, and each stator has six magnetic poles. The magnetic poles of the left stator are A11, A12, B11, B12, C11, and C12, and the magnetic poles of the right stator are A21, A22, B21, B22, C21, and C22. When the rotor is in the equilibrium position, the bias flux of each air gap is equal, and the flow direction is radial. Taking the A phase as an example, the winding modes of coils A11 and A12 are opposite. When the positive current enters the A phase, the control flux generated by the control coil is in the same direction as the bias flux. The control flux generated by the control coil A12 is reverse to the bias flux. The magnetic flux of the magnetic pole A11

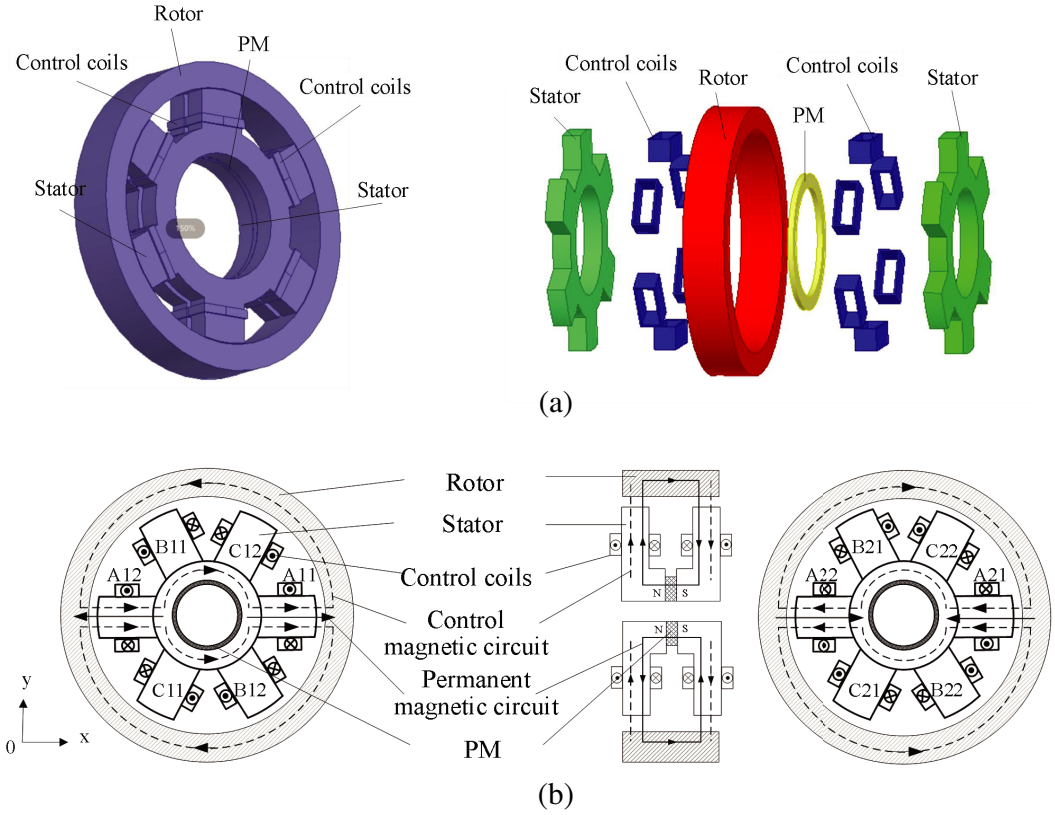

Figure 1. Structure and magnetic flux paths of OSHMB. (a) 3D model of OSHMB. (b) Magnetic flux paths of OSHMB.

is the superposition of two kinds of magnetic flux, and the magnetic pole A12 is offset the two kinds of magnetic flux of the air gap. Therefore, the suspension force between the rotor and magnetic pole A11 will be produced. Similarly, when the negative current enters the A phase, the suspension force is generated along the magnetic pole A12. Note that the bias flux flow on the left stator is opposite to that on the right stator, so the coil winding mode of the right stator coil A11 and the coil winding mode of the left stator coil A21 are opposite. Each coil winding and working principle of B, C phases are the same. Hence, by changing the value of each phase current, a three-phase inverter can be used to drive the radial two-degree-of-freedom to control the dual-chip radial-axial SHMB.

The magnetic circuit diagram shown in Figure 2 can be obtained from Figure 1(b). Assume that rotor radial displacements are x and y:

$$\begin{cases} \Phi_{A11} = \Phi_{A21} = \dfrac{\mu_0 S_r}{\delta_r - x} \cdot \dfrac{F_m}{2} + \dfrac{\mu_0 S_r}{\delta_r - x} \cdot \dfrac{Ni_A}{4} \\ \Phi_{A12} = \Phi_{A22} = \dfrac{\mu_0 S_r}{\delta_r + x} \cdot \dfrac{F_m}{2} - \dfrac{\mu_0 S_r}{\delta_r + x} \cdot \dfrac{Ni_A}{4} \\ \Phi_{B11} = \Phi_{B21} = \dfrac{\mu_0 S_r}{\delta_r + 0.5x - \sqrt{3}y/2} \cdot \dfrac{F_m}{2} + \dfrac{\mu_0 S_r}{\delta_r + 0.5x - \sqrt{3}y/2} \cdot \dfrac{Ni_B}{4} \\ \Phi_{B12} = \Phi_{B22} = \dfrac{\mu_0 S_r}{\delta_r - 0.5x + \sqrt{3}y/2} \cdot \dfrac{F_m}{2} - \dfrac{\mu_0 S_r}{\delta_r - 0.5x + \sqrt{3}y/2} \cdot \dfrac{Ni_B}{4} \\ \Phi_{C11} = \Phi_{C21} = \dfrac{\mu_0 S_r}{\delta_r + 0.5x + \sqrt{3}y/2} \cdot \dfrac{F_m}{2} + \dfrac{\mu_0 S_r}{\delta_r + 0.5x + \sqrt{3}y/2} \cdot \dfrac{Ni_C}{4} \\ \Phi_{C12} = \Phi_{C22} = \dfrac{\mu_0 S_r}{\delta_r - 0.5x - \sqrt{3}y/2} \cdot \dfrac{F_m}{2} - \dfrac{\mu_0 S_r}{\delta_r - 0.5x - \sqrt{3}y/2} \cdot \dfrac{Ni_C}{4} \end{cases} \quad (1)$$

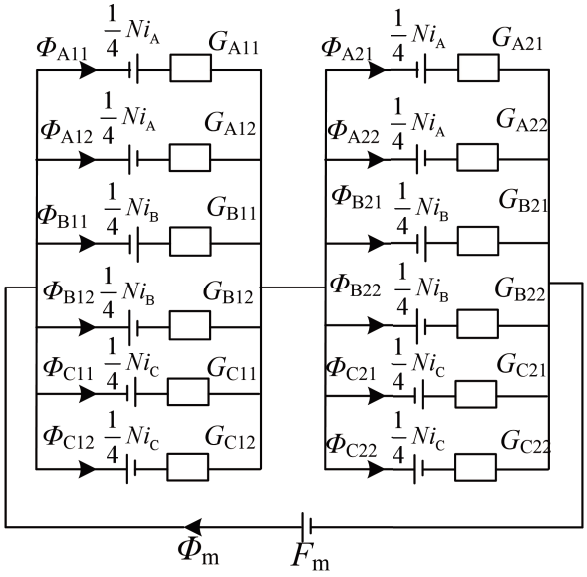

Figure 2. Equivalent magnetic circuit of the SHMB.

where Φ_{A11}, Φ_{A12}, Φ_{A21}, Φ_{A22}, Φ_{B11}, Φ_{B12}, Φ_{B21}, Φ_{B22}, Φ_{C11}, Φ_{C12}, Φ_{C21}, Φ_{C22} are flux of each pole; N is the total number of turns per phase coil; Φ_m in the diagram is total bias flux; F_m is the magnetic dynamic potential of the permanent magnet; i_A, i_B, i_C are inverter currents; δ_r is the radial air gap length; S_r is the magnetic pole area; μ_0 is the vacuum permeability.

From the flux of Equation (1):

$$F_j = \left(\frac{\Phi_{j11}^2}{2\mu_0 S_r} - \frac{\Phi_{j12}^2}{2\mu_0 S_r} \right) \times 2 \quad (j = \text{A, B, C}) \tag{2}$$

Equation (2) is linearized to:

$$\begin{cases} F_{\text{A}} = k_{xy} \cdot x + k_{ir} \cdot i_{\text{A}} \\ F_{\text{B}} = -\dfrac{1}{2} k_{xy} \cdot x + \dfrac{\sqrt{3}}{2} k_{xy} \cdot y + k_{ir} \cdot i_{\text{B}} \\ F_{\text{C}} = -\dfrac{1}{2} k_{xy} \cdot x - \dfrac{\sqrt{3}}{2} k_{xy} \cdot y + k_{ir} \cdot i_{\text{C}} \end{cases} \tag{3}$$

where $k_{xy} = \frac{\mu_0 S_r F_m^2}{\delta_r^3}$ is the radial force/displacement stiffness, and $k_{ir} = \frac{\mu_0 S_r F_m N}{2\delta_r^2}$ is the radial force/current stiffness.

The suspension force model is obtained by 3/2 transformation of Equation (3):

$$\begin{bmatrix} F_x \\ F_y \end{bmatrix} = \frac{3}{2} k_{xy} \cdot \begin{bmatrix} 1 & 0 \\ 0 & 1 \end{bmatrix} \begin{bmatrix} x \\ y \end{bmatrix} + k_{ir} \begin{bmatrix} 1 & -\dfrac{1}{2} & -\dfrac{1}{2} \\ 0 & \dfrac{\sqrt{3}}{2} & -\dfrac{\sqrt{3}}{2} \end{bmatrix} \begin{bmatrix} i_{\text{A}} \\ i_{\text{B}} \\ i_{\text{C}} \end{bmatrix} \tag{4}$$

When the maximum current $i_{\max}$ enters the magnetic pole A11, the magnetic flux of magnetic pole A11 reaches saturation magnetic induction intensity B_s, and the magnetic flux of magnetic pole A12 is 0 T. The maximum suspension force in the positive direction of the x axis:

$$\begin{cases} \Phi_{A11} = \Phi_{r0} + k_{ir} i_{r\max} = B_s S_r \\ \Phi_{A12} = \Phi_{r0} - k_{ir} i_{r\max} = 0 \end{cases} \tag{5}$$

From Equation (5):

$$\Phi_{r0} = k_{ir} i_{r\max} = \frac{1}{2} B_s S_r \tag{6}$$

The magnetic fluxes in the air gaps of B11, B12, C11, C12 are:

$$\begin{cases} \Phi_{\mathrm{B11}} = \Phi_{r0} - \dfrac{1}{2}k_{ir}i_{r\max} = \dfrac{1}{4}B_sS_r \\ \Phi_{\mathrm{B12}} = \Phi_{r0} + \dfrac{1}{2}k_{ir}i_{r\max} = \dfrac{3}{4}B_sS_r \\ \Phi_{\mathrm{C11}} = \Phi_{r0} - \dfrac{1}{2}k_{ir}i_{r\max} = \dfrac{1}{4}B_sS_r \\ \Phi_{\mathrm{C12}} = \Phi_{r0} + \dfrac{1}{2}k_{ir}i_{r\max} = \dfrac{3}{4}B_sS_r \end{cases} \tag{7}$$

Because the stator is two-piece, the maximum suspension force in the x direction is obtained:

$$F_{x\max} = 2\left(F_{\mathrm{A11}} - F_{\mathrm{A12}} - \frac{1}{2}F_{\mathrm{B11}} + \frac{1}{2}F_{\mathrm{B12}} - \frac{1}{2}F_{\mathrm{C11}} + \frac{1}{2}F_{\mathrm{C12}}\right) = \frac{3B_s^2S_r}{2\mu_0} \tag{8}$$

$$F_{y\max} = 2\left(\frac{\sqrt{3}}{2}F_{\mathrm{B11}} - \frac{\sqrt{3}}{2}F_{\mathrm{B12}} - \frac{\sqrt{3}}{2}F_{\mathrm{C11}} + \frac{\sqrt{3}}{2}F_{\mathrm{C12}}\right) = \frac{\sqrt{3}B_s^2S_r}{\mu_0} \tag{9}$$

3. MULTI-OBJECTIVE OPTIMIZATION OF SIX-POLE HYBRID MAGNETIC BEARING

Because the design results of the radial magnetic bearing prototype are directly related to the final volume, working stability, maximum suspension force of the bearing, and the parameters of the radial magnetic bearing must be designed reasonably.

As shown in Figure 3, the parameters of six pole outer rotor hybrid magnetic bearing need to be optimized, where b_n is the magnetic pole root width, d_2 the stator yoke inner diameter, d_1 the stator yoke outer diameter, r_3 the rotor outer radius, r_1 the polar shoe outer radius, r_2 the polar shoe inner radius, and b_m the polar shoe width. The x-direction suspension force F and volume V of the six-pole rotor magnetic bearing are used as the objective function. The parameters of the six-pole outer rotor hybrid magnetic bearings are optimized for multiple objectives [28].

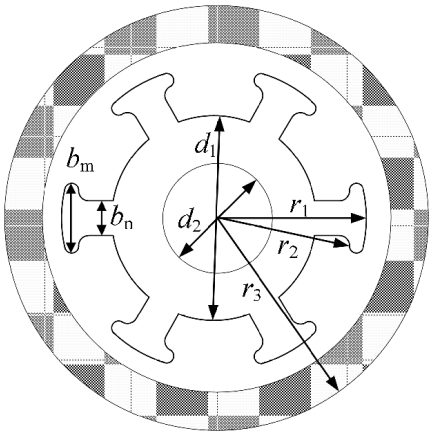

Figure 3. Parameters of the outer rotor six-pole magnetic bearing.

3.1. Sensitivity Analysis

The optimized parameters and their ranges of values are first determined as shown in Table 1 below, and the initial optimization parameters of the six-pole outer rotor hybrid magnetic bearing are up to 8, which will lead to a substantial increase in the number of multi-objective optimization samples.

Table 1. Optimize the variables and their range of values.

name	parameter	minimum (mm)	maximum (mm)
Magnetic polar root width	b_n	6	24
Magnetic pole shoe width	b_m	22	26
The inner diameter of the stator yoke	d_2	38	58
The outer diameter of the stator yoke	d_1	80	84
Outer radius of the stator pole shoe	r_1	58.5	60.5
inner radius of the stator pole shoe	r_2	54.5	58.5
The outer radius of the rotor	r_3	69	73
Thickness of stator	l_1	8	12

To reduce the computational amount and the design space, the first step in the optimization is the sensitivity analysis. The sensitivity index of the optimized parameters can be expressed as:

$$\bar{S}_{ni}^{m} = \frac{\partial f}{\partial z_i}\bigg|_{\mathrm{NOP}} \frac{z_i}{f} \approx \frac{\Delta f/f}{\Delta z_i/z_i} \tag{10}$$

where z_i represents the optimization parameters; f is the optimization objective.

The sensitivity analysis of Figure 4 is obtained. b_n, b_m, l_1, and r_2 are even more significant than other parameters. Notably, this analysis cannot be applied to the global space because it is a local sensitivity analysis. Therefore, the values of non-significant variables can be determined by an optimization method of parametric scanning and weighting, while the determination of significant variables requires the application of other optimization methods.

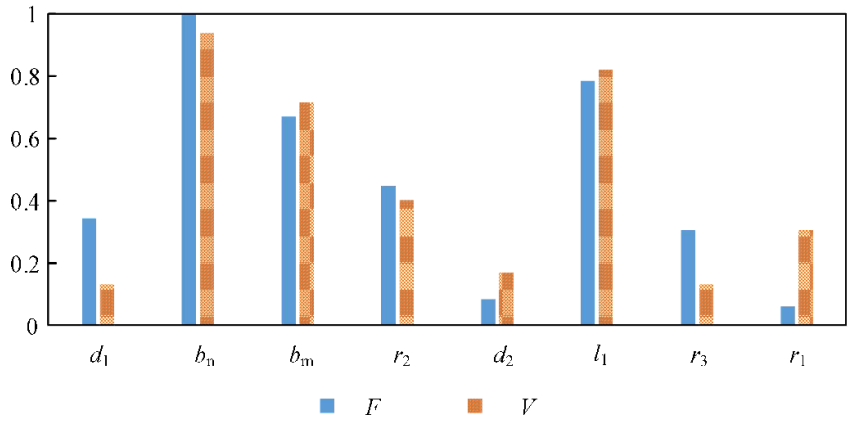

Figure 4. Sensitivity indices of the design variables.

3.2. Construction of the Response Face Model

Response Surface Method (RSM) is a method to obtain the optimal design variable and optimize the objective function by constructing the relationship between the design variable and the objective function. The Box-Behnken Design (BBD) method is a classic and commonly used method for experimental design. The method is suitable for modeling response faces with 2 to 5 factors. There are 3 levels for each factor in the BBD method, respectively, -1, 0, and 1, where 0 is the central point, and 1 and -1 correspond to the maximum and minimum values, respectively. The three levels of the four significant optimization parameters obtained from the sensitivity analysis are given in Table 2. In the BBD design, the number of design variables directly determines the number of trials. In the Design

Table 2. The level of the optimized parameters.

Level	−1	0	1
r_2 (mm)	54.5	56.5	58.5
b_m (mm)	22	24	26
l_1 (mm)	8	10	12
b_n (mm)	8	16	24

Table 3. This site is sampled by the BBD.

Run serial number	r_2 (mm)	l_1 (mm)	b_n (mm)	b_m (mm)
1	56.5	10	24	26
2	58.5	12	16	24
3	56.5	8	16	22
4	56.5	12	24	24
5	54.5	10	8	24
6	58.5	8	16	24
7	56.5	10	16	24
8	54.5	10	16	22
9	56.5	8	16	26
10	56.5	10	16	24
11	56.5	10	16	24
12	58.5	10	16	26
13	54.5	12	16	24
14	56.5	10	8	26
15	56.5	10	8	22
16	56.5	8	8	24
17	54.5	10	24	24
18	56.5	10	16	24
19	56.5	10	24	22
20	58.5	10	8	24
21	54.5	8	16	24
22	56.5	12	16	22
23	58.5	10	24	24
24	56.5	12	16	26
25	56.5	10	16	24
26	56.5	12	8	24
27	58.5	10	16	22
28	54.5	10	16	26
29	56.5	8	24	24

Expert software, according to the BBD method, 29 sets of experiments are required due to the presence of four optimization parameters. The selection of the 29 sample points is shown in Table 3. These 29 sets of trials are performed in the finite element analysis software.

In this paper, the finite element simulation results are analyzed using Design Expert software. Different models are used to fit the functional relationship between the objective function and the

optimization parameters.

The response surface model is obtained based on the relationship between the optimization parameters at the sample point and the finite element simulation results of the objective function. The x-direction suspension force of the objective function is expressed as:

$$\begin{aligned} F = {} & 16211.13664 - 510.18265 * r_2 - 92.54261 * l_1 - 173.03233 * b_m + 63.29170 * b_n \\ & + 2.57431 * r_2 * l_1 + 9.53180 * r_2 * bm - 0.56276 * r_2 * b_n + 2.29834 * l_1 * b_m \\ & + 1.78170 * l_1 * b_n + 0.10887 * b_m * b_n + 2.43361 * r_2^2 - 5.58268 * l_1^2 - 8.23099 * b_m^2 - 1.32098 * b_n^2 \end{aligned} \quad (11)$$

The volume of the objective function is expressed as:

$$V = 18981.3 + 15072 * l_1 + 702 * l_1 * b_m - 492 * l_1 * b_n - 12 * l_1 * r_2 * b_m + 12 * l_1 * r_2 * b_n \quad (12)$$

The response surface of the objective function regarding the optimization parameters is shown in Figure 5. It can be seen from Figure 5 that the optimal solution can be obtained for each objective function within a certain range of parameters; however, when each objective function obtains the optimal solution, the value range of the optimization variable is very different. Therefore, to avoid conflicts between objective functions, Pareto optimal solutions must be obtained using a multi-objective intelligent optimization algorithm.

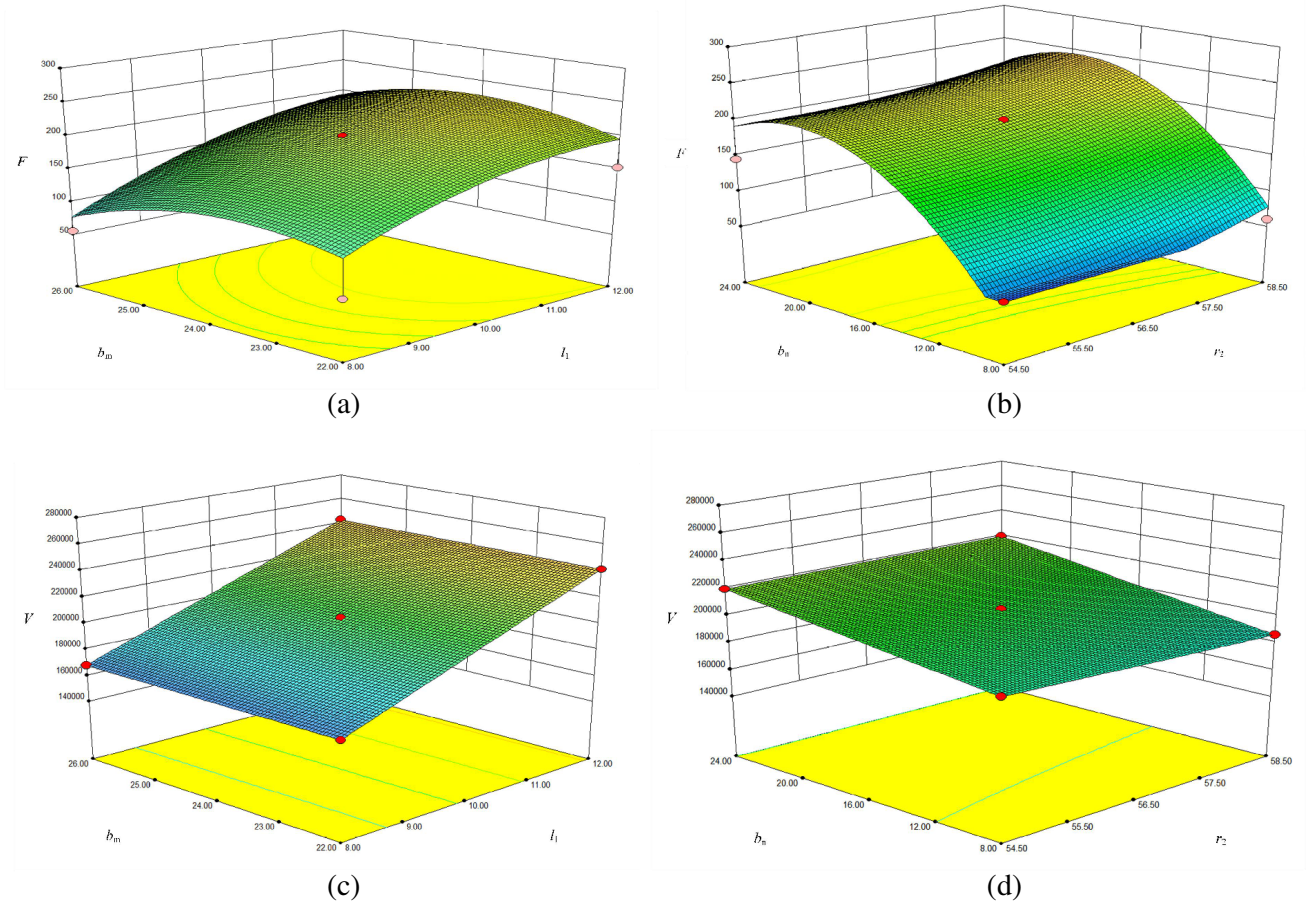

Figure 5. Response surfaces of optimization objective volume of suspension force in x direction F and the six-pole rotor outer magnetic bearing V.

3.3. Multi-Objective Optimization Based on Genetic Algorithms

The optimized design of magnetic bearings is a nonlinear optimization problem involving multi-objectives, for which there is a compromise set, none better than others without preference information.

Therefore, it is very important to introduce intelligent algorithms in multi-objective optimization problems, which can simultaneously process a set of possible solutions in a single operation and can achieve the trade-off design between the optimization objectives.

A genetic algorithm is used to optimize the two optimization targets according to the regression equations obtained by the response surface approach. The whole optimization process can be completed in a very short time, while a single parameter optimization simulation usually takes several hours using the finite element analysis software. The Pareto front of the x-direction suspension force F and the volume V of the six-pole outer rotor magnetic bearing is shown in Figure 6. The selected optimal solution is shown as red dots in Figure 6, when the x-direction suspension force F is 223.3 N, and the volume V of the six-pole outer rotor magnetic bearing is $2.12 \times 10^5\,\text{mm}^3$. The respective parameter values for the initial and optimal design are given in Table 4.

Table 4. Design variables.

Parameter	Initial design values/mm	Optimized values/mm
Magnetic polar shoe width	24	25.51
Magnetic pole root width	24	16.74
Thickness of stator	8	10.25
Magnetic pole inner radius	58.5	56.59
Outer diameter of stator yoke	82	82
The length of air gap	0.5	0.5
Radial pole area	262	288
Outer diameter of rotor	142	144
Inter diameter of rotor	118	118
Axial length of rotor	23	23
Coil turns	160	160
Outer diameter of PM	72	72
Inter diameter of PM	58	58
Axial length of PM	3	3
Inter diameter of stator yoke	58	54

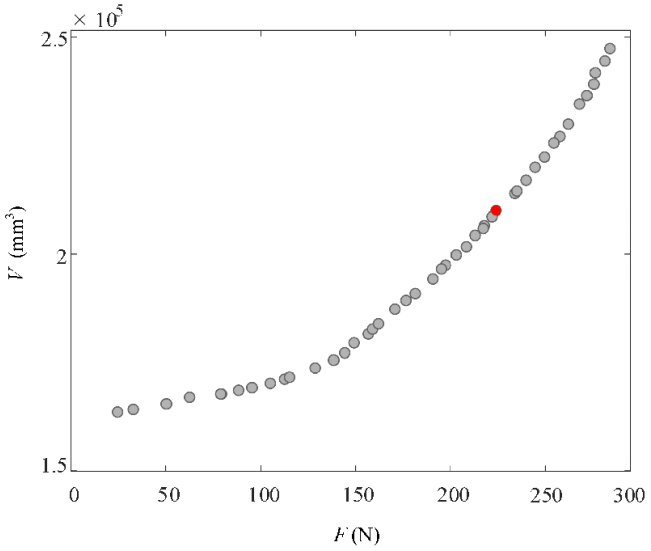

Figure 6. Pareto fronts.

4. FINITE ELEMENT ANALYSIS OF THE OSHMB

According to the design requirements of radial maximum bearing capacity of OSHMB, the key parameters of OSHMB are designed. According to the parameters of Table 4, the physical model of magnetic bearing is established by using ansoft software, and the theoretical design results are simulated to analyze the distribution of magnetic force line and flux density.

Figure 7(a) and Figure 7(c) show the magnetic induction intensity distribution of the OSHMB under the action of permanent magnet. At the same time, the bias flux of each air gap is 0.4 T, which is in accordance with the design requirements. Figure 7(b) and Figure 7(d) are the magnetic induction intensity distribution when the maximum current $i_{\max}$ enters the A phase coil. The maximum magnetic induction intensity of A11 is about 0.8 T, and the magnetic induction intensity of A12 is 0 T. Besides, since the B and C phase currents are both $-0.5i_{\max}$, the magnetic induction intensities of C12 and C11 are 0.6 T and 0.2 T, respectively. This is consistent with the theoretical analysis. In addition, under the condition of maximum current, the air gap flux is not saturated, and the OSHMB is designed in accordance with the design.

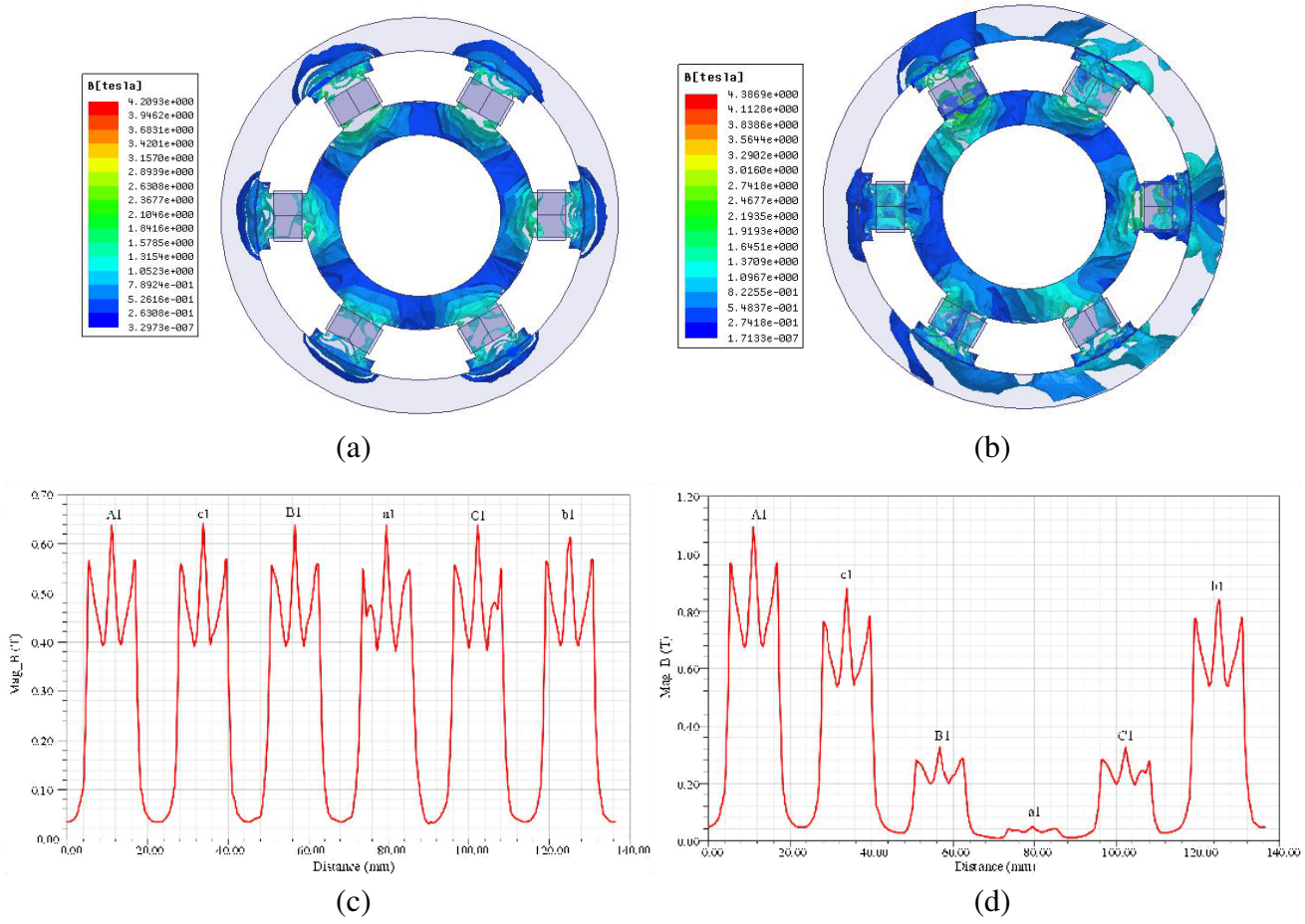

Figure 7. Magnetic flux density. (a) Magnetic density distribution when the control current is 0 A. (b) Magnetic density distribution when the control current is 1 A. (c) Magnetic density distribution of the air gap when the control current is 0 A. (d) Magnetic density distribution of the air gap when the control current is 1 A.

At the equilibrium position of the rotor, the simulation characteristic curves of the current of the OSHMB are shown in Figure 8(a) and Figure 8(b). We can see from Figure 8(a) and Figure 8(b) that the relationship between F_x and i_x is linear, and there is no coupling between F_x and i_x. Similarly, there is a linear relationship between F_y and i_y, and there is no coupling.

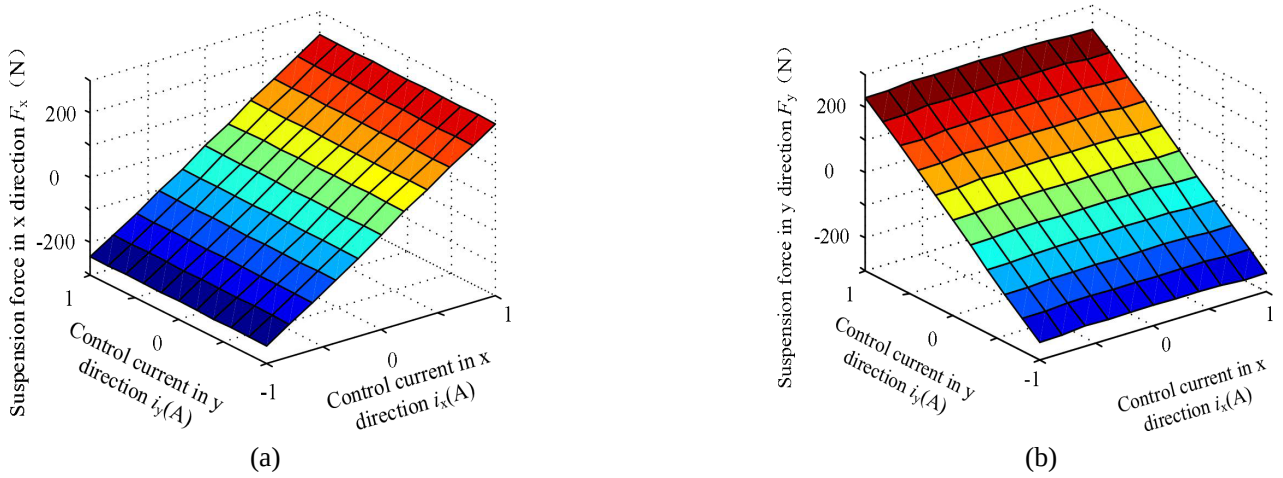

Figure 8. Relationship curve. (a) Curves between Fx and ix, iy of couple-piece type radial-axial six-pole HMB. (b) Curves between Fy and ix, iy of couple-piece type radial-axial six-pole HMB.

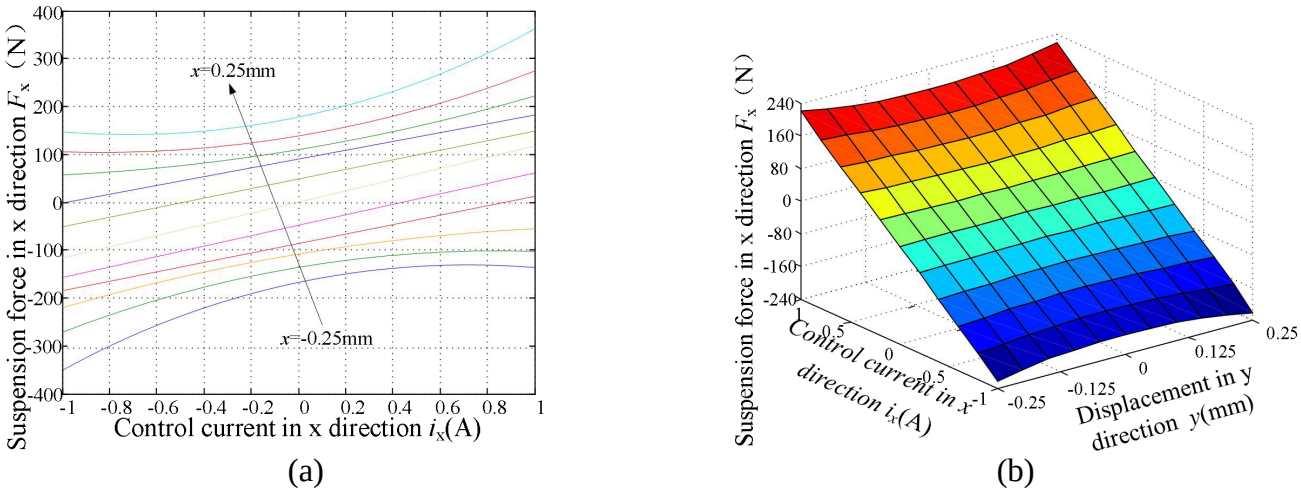

Figure 9. Influence of displacement x, y on the Fx-ix curves. (a) Effect of x on Fx-ix relation curve. (b) Effect of y on Fx-ix relation curve.

Then, taking the suspension force in the x axis as an example, when the displacement changes in the x direction, the relationship curve between F_x and i_x is analyzed. Figure 9(a) shows the relationship between F_x and i_x with the rotor at a certain displacement x. We can see from Figure 9(a) that when the displacement x is in the range of 0.1 mm, the curve between F_x and i_x can be considered as linear. Only when the displacement exceeds 0.15, the curve between F_x and i_x is obviously bent. The bending degree of the curve becomes more obvious with the increase of i_x. Figure 9(b) shows the relationship between F_x and i_x with the rotor at a certain displacement y. We can see from Figure 9(b) that the curve between F_x and i_x can be considered as a linear relationship, but the slope of the curve between F_x and i_x is partially changed, and the slope increases with the increase of y.

Because of the structural asymmetry of three-pole magnetic bearing, there is electromagnetic coupling between radial two degrees of freedom of the three-pole magnetic bearing, and there is nonlinear problem of force-current characteristic. Compared with the three-pole magnetic bearing, due to the symmetry of the six-pole structure, according to the above simulation analysis, it can be seen that the OSHMB can be regarded as linear, and the coupling degree is low, but it may be nonlinear under the condition that the rotor produces large displacement, such as fluctuation and excessive disturbance.

Simulation results are consistent with theoretical analysis. It is proved that the OSHMB has a broad application prospect.

5. PROTOTYPE AND EXPERIMENT

5.1. Experimental Platform and Control Strategy

In order to verify the accuracy of the above analysis results and further analyze the performance of the OSHMB, an experimental platform is designed and manufactured as shown in Figure 10. The experimental platform is mainly composed of eddy current displacement sensor, displacement signal interface circuit, digital signal processing (DSP) controller minimum system, DC power supply, radial power drive board, axial power drive board, AC power supply, PC machine, and DSP controller.

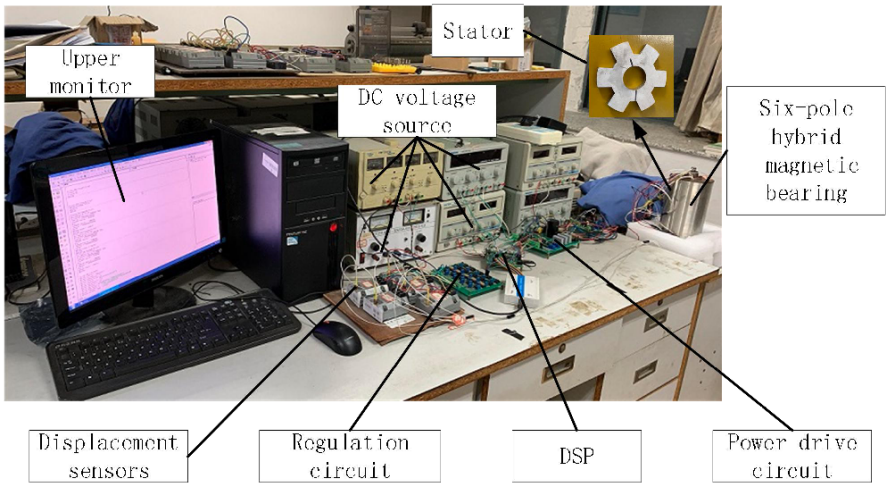

Figure 10. Experimental platform.

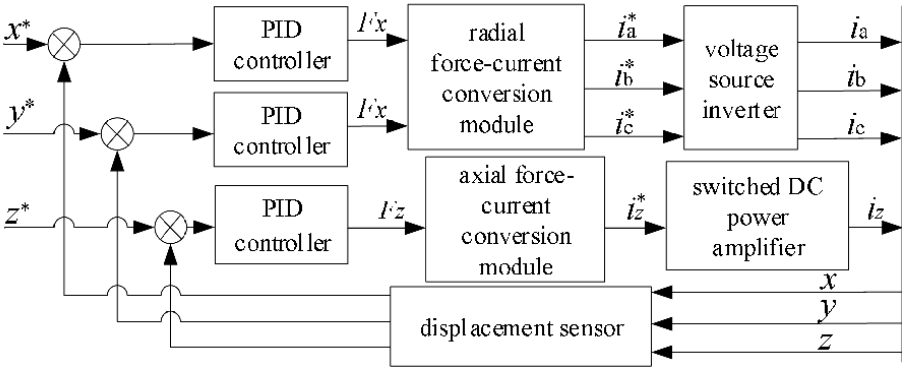

Figure 11. Control block diagram of magnetic bearing system.

The block diagram of the magnetic bearing control system is shown in Figure 11, and the mathematical model of suspension force is embodied in the force-current conversion module. The magnetic bearing itself is unstable, so the closed loop control system is used, and the real-time performance of the system is improved. If the rotor is shifted to the equilibrium position by external interference, and the displacement signal (x, y, z) of the rotor generated in the radial and axial direction can be obtained by the radial and axial displacement sensor, a displacement signal is then fed into the radial, axial proportional integral derivative (PID) controller. Radial PID controller outputs radial

force signal (F_x, F_y) to radial force-current conversion module, then the force-current conversion module outputs a three-phase control current reference signal for radial magnetic bearings (i_a^*, i_b^*, i_c^*), processing through the inverter, control currents (i_a, i_b, i_c) of three-phase control coils of drive radial magnetic bearing can be obtained.

5.2. Verification Experiment

5.2.1. Magnetic Bearing Capacity Test

When the maximum control current in the positive direction of the x axis is inserted into the radial control coil, the rotor moves. There are two forces acting on the rotor. One is the maximum suspension force in the positive direction of the x axis, and the other is the force generated by the rotor eccentricity. The force F_1 is the force of maximum suspension force and rotor eccentricity force when the rotor is pulled. Moving the rotor to the stator in the positive direction of the x-axis, then removing the control current and drag the rotor in the negative direction of the x-axis by using the spring dynamometer, the value of the spring dynamometer is the value of the force generated by the rotor eccentricity F_2 when the rotor is dragged. The difference between F_1 and F_2 is the maximum bearing capacity of the magnetic bearing in the x positive direction of the shaft. The maximum bearing capacity of the OSHMB and the original designed magnetic bearing measured by the above method is shown in Table 5.

Table 5. Maximum bearing capacity.

Magnetic bearing	The direction of maximum suspension force	Calculation/N	Simulation/N	Experiment/N
OSHMB	x-axis	220	223.3	239
	y-axis	253	242	266
SHMB	x-axis	200	202	218
	y-axis	230	219	251

It can be seen from the table that the experimental results are relatively larger than the simulation and calculation results. The maximum suspension force of the magnetic bearing is determined by the smaller force of the maximum suspension force in the x and y directions. The maximum suspension force of the OSHMB is 239 N in the x direction, and the maximum suspension force of the SHMB is 218 N in the x direction. It can be seen that the maximum bearing capacity of the OSHMB is about 9.6% higher than that of the original designed six-pole hybrid magnetic bearing. At the same time, the experimental results are similar to the simulation and calculation results, which proves the correctness of the theoretical analysis.

5.2.2. Nonlinear Experiment of Suspension Force

In order to verify the relationship between the radial suspension force and radial control current of the magnetic bearing, the relationship between the suspension force and the current can be approximately measured by the method of bearing capacity experiment. In the nonlinear experiment of suspension force, a large amount of experimental data is collected and recorded. In view of the large amount of test data and repeated test process, the data listed for each test are only for reference. Through statistical analysis, the data are drawn into curves, and the comparison between finite element results and experimental results can be clearly seen. Figure 12 shows the relationship curve between the suspension force in the x direction and the control current in the x direction. The calculated results and finite element results are in good agreement with the experimental results, and the accuracy of the electromagnetic characteristic analysis is verified. As shown in Figure 12, the suspension force of the OSHMB is linearly related to the control current in the x axis.

Experimental results show that the OSHMB solves the problem of nonlinear characteristics of the three-pole hybrid magnetic bearing.

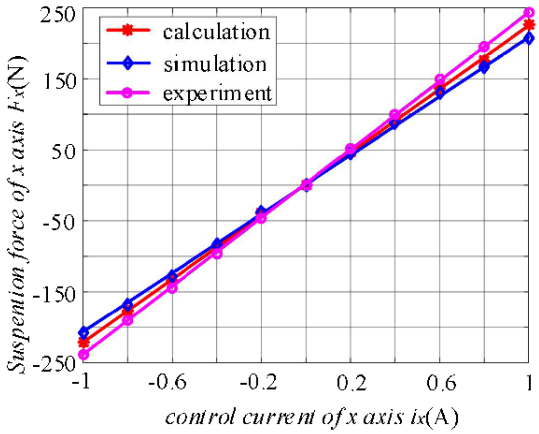

Figure 12. x-axis suspension force-current characteristic curves.

5.2.3. Magnetic Coupling Test

The relationship between the suspension force in the x direction and the control current in the y direction is obtained by measuring the suspension force in the bearing capacity experiment as shown in Figure 13. We can see from Figure 13(a) and Figure 13(b) that the suspension force in the x axis is not affected by the control current in the y axis, and the suspension force in the y axis is not affected by the control current in the x axis. There is no magnetic circuit coupling between radial two degrees of freedom.

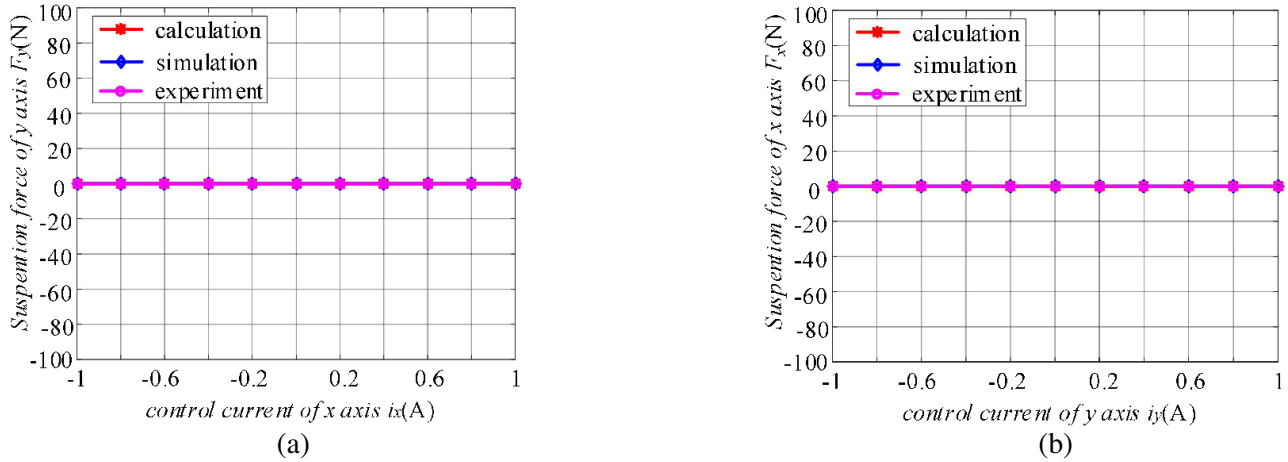

Figure 13. (a) The relationship between y-axis suspension force and x-axis current. (b) The relationship between x-axis suspension force and y-axis current.

5.3. Suspension Experiments of OSHMB

5.3.1. Floating Experiments

Figure 14 shows the displacement waveform of the rotor when the OSHMB rotor floats. It can be seen from the diagram that the magnetic bearing rotor reaches the equilibrium position from the auxiliary bearing after 0.04 seconds and stabilizes the suspension.

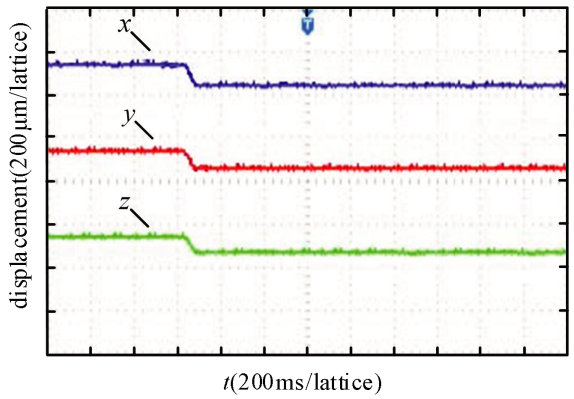

Figure 14. The waveform of rotor floatation.

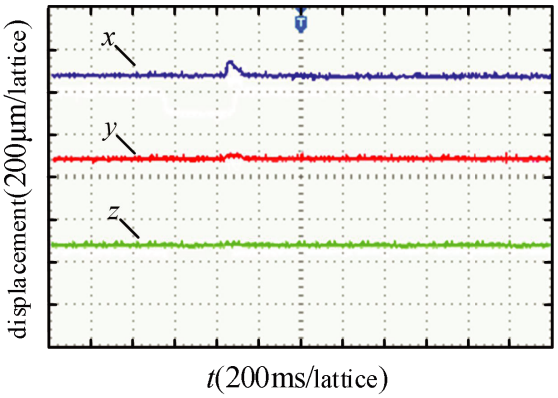

Figure 15. The waveform of rotor disturbance.

5.3.2. Anti-Disturbance Experiment

Figure 15 shows the displacement waveform of the rotor when the rotor of the OSHMB is disturbed. When the rotor is suspended stably in the equilibrium position, 100 N of instantaneous disturbance is applied to the rotor in the x direction, and the rotor deviates from the equilibrium position. When the external disturbance force disappears, the rotor quickly returns to the equilibrium position under the action of the control current. We can see from Figure 15 that the rotor will deviate from the equilibrium position under the action of the external disturbance force in the x direction, and the disturbance in the x direction will have a slight effect in the y axis and almost no effect in the z direction. The anti-interference experiment shows that the OSHMB has good anti-interference ability.

5.3.3. Load Experiments

When the system is in a steady state, a y-direction disturbance is applied to the rotor, and the weight is suspended at one end of the rotor for the purpose of applying a 100 N disturbance to the rotor. Figure 16(a) indicates the rotor displacement in the x-direction. Figure 16(b) indicates the rotor displacement in the y-direction when disturbed. As can be seen from Figure 16, the displacement in the x direction shifts slightly when the rotor in the y direction is disturbed, and the rotor displacement offset of the OSHMB in the y direction is approximately 200 μm while the recovery time of the OSHMB in the y direction is approximately 120 ms. The experimental results show that the OSHMB has good anti-interference performance.

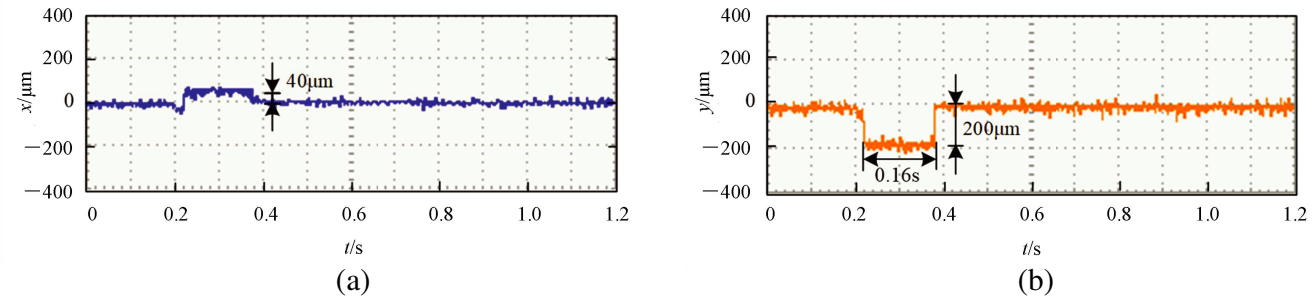

Figure 16. The experiment results of adding load. (a) Displacement waveform in the x direction of OSHMB. (b) Displacement waveform in the y direction of OSHMB.

5.3.4. Dynamic Suspension Experiment

Figure 17 shows the suspension experiment at different speeds. The blue waveform is the displacement waveform in the x direction; the red waveform is the displacement waveform in the y direction; the abscissa is the time coordinates, 20 ms per lattice; the ordinate is the displacement coordinates, 200 μm per lattice, at the front of 120 ms, the displacement waveform at 3600 rpm; at the rear of 120 ms, the displacement waveform at 1800 rpm. It can be seen from Figure 17 that both the maximum amplitudes of the displacement waveform in the x and y directions are 100 μm, which is far smaller than the length of the gas gap. The rotor suspension is stable at different speeds.

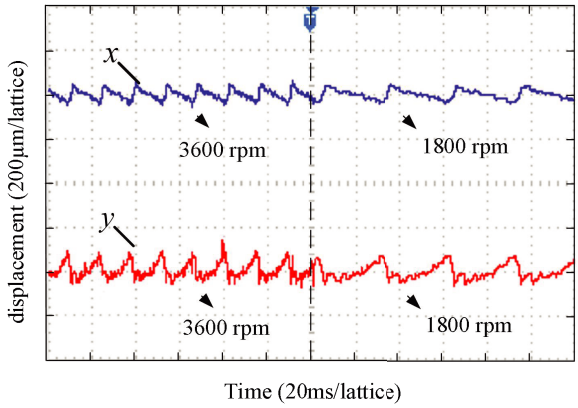

Figure 17. Rotor displacement at different speeds.

6. CONCLUSION

In order to improve the performance of the six-pole external rotor hybrid magnetic bearings, an optimal set of parameters is obtained by sensitivity analysis, construction of a response surface model, and multi-objective optimization based on the genetic algorithm. The key parameter stator yoke internal diameter is 56.59 mm; stator thickness is 10.25 mm; magnetic polar boot width is 25.51 mm; and magnetic pole root width is 16.74 mm. After simulation according to the optimized parameters, the relationship between F_x and i_x is linear, and there is no coupling between F_x and i_x. Similarly, there is a linear relationship between F_y and i_y. It can be seen that the maximum bearing capacity of the OSHMB is about 9.6% higher than that of the SHMB. At the same time, the experimental results are similar to the simulated and calculation results, which proves the correctness of the theoretical analysis.

REFERENCES

1. Gu, H., H.-Q. Zhu, and Y.-Z. Hua, "Soft sensing modeling of magnetic suspension rotor displacements based on continuous hidden markov model," *IEEE Transactions on Applied Superconductivity*, Vol. 28, No. 3, 1–5, Apr. 2018.
2. Le, Y. and K. Wang, "Design and optimization method of magnetic bearing for high-speed motor considering eddy current effects," *IEEE/ASME Transactions on Mechatronics*, Vol. 21, No. 4, 2061–2072, Aug. 2016.
3. Usman, I., M. Paone, K. Smeds, and X. Lu, "Radially biased axial magnetic bearings/motors for precision rotary-axial spindles," *IEEE/ASME Transactions on Mechatronics*, Vol. 16, No. 3, 411–420, Jun. 2011.
4. Abooee, A. and A. M. Arefi, "Robust finite-time stabilizers for five-degree-of-freedom active magnetic bearing system," *Journal of the Franklin Institute-Engineering and Applied Mathematics*, Vol. 356, 80–102, 2019.

5. Peng, C., J. Sun, X. Song, and J. Fang, "Frequency-varying current harmonics for active magnetic bearing via multiple resonant controllers," *IEEE Transactions on Industrial Electronics*, Vol. 64, No. 1, 517–526, Jan. 2017.
6. Gu, H., H. Zhu, and Y. Hua, "Soft sensing modeling of magnetic suspension rotor displacements based on continuous hidden Markov model," *IEEE Transactions on Applied Superconductivity*, Vol. 28, No. 3, 1–5, Apr. 2018.
7. Yu, J. and C. Zhu, "A multifrequency disturbances identification and suppression method for the self-sensing AMB rotor system," *IEEE Transactions on Industrial Electronics*, Vol. 65, No. 8, 6382–6392, Aug. 2018.
8. Zhang, W.-Y., H.-Q. Zhu, Z.-B. Yang, X.-D. Sun, and Y. Yuan, "Nonlinear model analysis and "switching model" of AC-DC three degree of freedom hybrid magnetic bearing," *IEEE/ASME Transactions on Mechatronics*, Vol. 21, No. 2, 1102–1115, Apr. 2016.
9. Zhang, W.-Y., H.-K. Yang, L. Cheng, and H.-Q. Zhu, "Modeling based on exact segmentation of magnetic field for a centripetal force type-magnetic bearing," *IEEE Transactions on Industrial Electronics*, Vol. 67, No. 9, 7691–7701, Sept. 2020.
10. Wang, S.-S., H.-Q. Zhu, M.-Y. Wu, and W.-Y. Zhang, "Active disturbance rejection decoupling control for three-degree-of-freedom six-pole active magnetic bearing based on BP neural network," *IEEE Transactions on Applied Superconductivity*, Vol. 30, No. 4, 1–5, Jun. 2020.
11. Ren, X.-J., M. Feng, and T.-M. Ren, "Design and optimization of a radial high-temperature superconducting magnetic bearing," *IEEE Transactions on Applied Superconductivity*, Vol. 29, No. 2, 1–5, Mar. 2019.
12. Wu, H., C.-G. Xu, D.-G. Xiao, and J. Hao, "Magnetic field analysis and optimal design of magnetic bearing," *2009 International Conference on Mechatronics and Automation*, 1666–1670, Changchun, 2009.
13. Yamagishi, K., "Optimum design of integrated magnetic bearing using multiple HTS bulk units," *IEEE Transactions on Applied Superconductivity*, Vol. 29, No. 5, 1–5, Aug. 2019.
14. Zhu, R., W. Xu, C. Ye, J. Zhu, G. Lei, and X. Li, "Design optimization of a novel heteropolar radial hybrid magnetic bearing using magnetic circuit model," *IEEE Transactions on Magnetics*, Vol. 54, No. 3, 1–5, Mar. 2018.
15. Xu, B., L. Zhang, and W. Ji, "Improved non-singular fast terminal sliding mode control with disturbance observer for PMSM drives," *IEEE Transactions on Transportation Electrification*, 2021.
16. Zhu, H. and T. Liu, "Rotor displacement self-sensing modeling of six-pole radial hybrid magnetic bearing using improved particle swarm optimization support vector machine," *IEEE Transactions on Power Electronics*, Vol. 35, No. 11, 12296–12306, Nov. 2020.
17. Fernandes, J. F.-P., A. J. A. Costa, and J. Arnaud, "Optimization of a horizontal axis HTS ZFC levitation bearing using genetic decision algorithms over finite element results," *IEEE Transactions on Applied Superconductivity*, Vol. 30, No. 2, 1–8, Mar. 2020.
18. Saha, S. and M. Nabi, "Control of axial active magnetic bearing using reduced order model," *2019 8th International Conference on Modeling Simulation and Applied Optimization (ICMSAO)*, 1–5, Manama, Bahrain, 2019.
19. Safaeian, R. and H. Heydari, "Optimal design of passive permanent magnet bearings," *2019 27th Iranian Conference on Electrical Engineering (ICEE)*, 458–463, Yazd, Iran, 2019.
20. Chen, Z., Z. Lin, C. Yue, and Y. Li, "Particle swarm optimized command filtered backstepping control for an active magnetic bearing system*," *2018 IEEE International Conference on Information and Automation (ICIA)*, 155–160, Wuyishan, China, 2018.
21. He, Y., X. He, J. Ma, and Y. Fang, "Optimization research on a switching power amplifier and a current control strategy of active magnetic bearing," *IEEE Access*, Vol. 8, 34833–34841, 2020.
22. Han, B.-C., Q.-J. Xu, and Q. Yuan, "Multiobjective optimization of a combined radial-axial magnetic bearing for magnetically suspended compressor," *IEEE Transactions on Industrial Electronics*, Vol. 63, No. 4, 2284–2293, Apr. 2016.

23. Chen, R., H. Li, and J. Tian, "The relationship between the number of poles and the bearing capacity of radial magnetic bearing," *2017 Chinese Automation Congress (CAC)*, 5553–5557, Jinan, 2017.
24. Quéval, L., G. G. Sotelo, and Y. Kharmiz, "Optimization of the superconducting linear magnetic bearing of a maglev vehicle," *IEEE Transactions on Applied Superconductivity*, Vol. 26, No. 3, 1–5, Apr. 2016.
25. Cansiz, A., İ. Yildizer, and D. T. McGuiness, "A case study for a superconducting magnetic bearing optimization," *2017 10th International Conference on Electrical and Electronics Engineering (ELECO)*, 1466–1470, Bursa, 2017.
26. Smirnov, A., N. Uzhegov, T. Sillanpää, J. Pyrhönen, and O. Pyrhönen, "High-speed electrical machine with active magnetic bearing system optimization," *IEEE Transactions on Industrial Electronics*, Vol. 64, No. 12, 9876–9885, Dec. 2017.
27. Liu, X. and B.-C. Han, "The multiobjective optimal design of a two-degree-of-freedom hybrid magnetic bearing," *IEEE Transactions on Magnetics*, Vol. 50, No. 9, 1–14, Sept. 2014.
28. Hua, Y.-Z., H.-Q. Zhu, M. Gao, and Z.-Y. Ji, "Multi-objective optimization design of permanent magnet assisted bearingless synchronous reluctance motor using NSGA-II," *IEEE Transactions on Industrial Electronics*, Vol. 68, No. 11, 10477–10487, Nov. 2021.